A Triptych Photocatalyst Based on the Co-Integration of Ag Nanoparticles and Carbo-Benzene Dye into a TiO 2 Thin Film

Jérémy Cure, Kévin Cocq, Adnen Mlayah, Teresa Hungría, Pierre Alphonse, Yves J Chabal, Valérie Maraval, Rémi Chauvin, Alain Estève, Carole Rossi

A Triptych Photocatalyst Based on the Co-Integration of Ag Nanoparticles and *Carbo*-Benzene Dye into a TiO_2 Thin Film

Jérémy Cure[1,*], *Kévin Cocq*[2], *Adnen Mlayah*[1,3], *Teresa Hungria*[4], *Pierre Alphonse*[5], *Yves J. Chabal*[6], *Valérie Maraval*[2], *Remi Chauvin*[2], *Alain Estève*[1], *Carole Rossi*[1,*]

[1]LAAS-CNRS, University of Toulouse, 7 avenue du colonel Roche, 31031 Toulouse, France

[2]LCC-CNRS, University of Toulouse, 205 route de Narbonne, 31077 Toulouse, France

[3]CEMES-CNRS, University of Toulouse, 29 rue Jeanne Marvig, 31055 Toulouse, France

[4]Centre de Microcaractérisation Raimond CASTAING, University of Toulouse, CNRS, UT3-Paul Sabatier, INP, INSA, Espace Clément Ader, 3 rue Caroline Aigle, 31400 Toulouse, France

[5]CIRIMAT, University of Toulouse, CNRS, UT3-Paul Sabatier, 118 route de Narbonne, 31062 Toulouse, France

[6]Department of Materials Science and Engineering, University of Texas at Dallas, Richardson, TX (USA)

Abstract

This work proposes a new efficient, long-lasting scalable and low-cost triptych photocatalyst by assembling a semiconductor thin film (planar anatase TiO_2), a photosensitive molecule (Cbz) of the *carbo*-benzene family and plasmonic Ag nanoparticles with exquisite degree of intimacy with the semiconductor. Under simulated sunlight conditions over 48 h, the triptych TiO_2/Ag/Cbz photocatalyst allows a hydrogen production rate of 0.18 $mmol.g_{photocatalyst}^{-1}.h^{-1}$ in conditions of applicative pressure (2.2 bars) and temperature (ambient) suitable for commercial applications. A ternary synergy (~33%) for hydrogen production is clearly evidenced with the triptych material in comparison with the diptych counterpart.

The role of each component (TiO_2, Ag and Cbz) on the H_2 production is investigated systematically by discriminating the light absorption from the different materials and interfaces. We show how to achieve an efficient vertical Schottky junction between Ag nanoparticles and the TiO_2 substrate that is demonstrated to be of crucial importance in the water-splitting process.

Keywords: *carbo*-benzene dye, silver nanoparticle, titanium dioxide film, triptych system, photocatalytic hydrogen production under pressure, water splitting

1. Introduction

Interest in hydrogen energy is greater than ever, notably because of the strong expectations for the development of new means of transport based on the improvement of fuel cell to cars, ships and even trains[1] to counterbalance the depletion of fossil fuels and global warming [2-4].

Alternately to water electrolysis and PhotoElectroCatalytic Water Splitting (PEC-WS) [5-9], achieving a pure PhotoCatalytic (PC) WS process from water and sunlight offers a promising approach for producing a sustainable costless and carbon free economy [10-13]. The PC-WS concept is simple: sun irradiates a powdered photocatalyst dispersed in an aqueous solution and the hydrogen is readily produced [14]. Rigorously, there is no need of a counter electrode, neither of a supporting electrolyte nor a pH-buffer: the photon energy is converted into electron-hole pairs and then into chemical energy [15].

The PC-WS concept has been validated with numerous semiconductor materials [16-18], and the majority of reports was based on Earth-abundant and stable semiconductors such as titanium dioxide (TiO_2) used for its moderate redox potential *vs* SHE (e.g. $E°_{1/2}(TiO_2/Ti^{2+})$= - 0.50 V), large bandgap (*E*g ~3.2 eV) and effective catalytic properties. However, the PC efficiency of semiconductors remains limited by several factors: (i) inability to harvest the visible light due to large band gap, only allowing the use of about 4% of the total solar radiation while the visible light contributes to *ca* 50% of the solar irradiance, (ii) fast recombination of photo-generated electron-hole pairs before they can migrate to the surface [19, 20]. Therefore, various strategies have been explored to improve the WS efficiency under solar illumination. The band gap can be narrowed and light absorption extended to longer wavelengths by doping with non-metal atoms [21, 22], with organic dyes [23] such as ruthenium complexes [24], porphyrins [25], or graphene oxide [26-29]. Another strategy to improve the PC efficiency relies on the use of hybrid metal

nanoparticles/semiconductor nanostructures [30-44], in order to reduce the electron-hole recombination and/or to harvest the visible light owing to plasmonic enhanced optical absorption [29, 30, 45]. Inorganic semiconductors based on transition-metal oxides, oxysulfides or oxynitrides with lower bandgap as compared to TiO_2 can also be used to increase the absorption of visible-light [10-12]. Finally, the formation of heterojunctions with other semiconductors (Bi_2WO_6, m-$BiVO_4$, TaON, Bi_2O_3, Ag_2O, Ag_3VO_4…) [46-51] has been proposed to induce beneficial charge separation and electronic properties in the stack.

Although significant advances have been achieved in the design of efficient materials for enhanced photocatalysis [52], the reported efficiencies are still far from those required for commercialization of operating devices.

Moreover, powdered photocatalysts, which have attracted a large attention in the past years and constitute the subject of most of the published works on PC-WS, suffer from the possible dispersion of particles into the environment and are not advantageous for large-scale production. Only a few concepts for scaling-up these technologies have been reported [53, 54]. One remarkable achievement in 2018 is the 1 m² flat panel reactor composed of Al-doped $SrTiO_3$ powder photocatalyst, achieving a solar-to-hydrogen energy conversion efficiency of 0.4% by WS [15], which is still too low for large-scale application of solar WS.

One challenge of solar to H_2 technology is the design of an efficient, long-lasting, scalable and low-cost photocatalyst, well-optimized for sunlight absorption to drive catalytic hydrogen evolution, which is the scope of the present study. The originality of the presented work is to assemble a triptych material (sparse examples in the literature) and demonstrate synergistic effects between its components. This is performed within a scalable, durable and low cost (mass fabrication compatible) technological pathway, based on a planar structure avoiding potential dissemination of nanoparticles in the environment. The hydrogen production is measured, for the

first time, under slightly over-pressurized conditions, which we believe are closer to those of the device operation in envisaged applications. Results are compared to values of the literature, all recorded at the atmospheric pressure, pointing to the need of further investigation of this issue.

In more detail, we combine in an optimized assembly, a light harversting semiconductor thin film (TiO_2) with efficient and low cost noble metal (Ag) and a *carbo*-benzene macromolecule to prepare a hybrid nanomaterial for H_2 generation by PC-WS. For the first time, a *carbo*-benzene macromolecule functionalized with two NH_2 –primary amino groups (*para*-di(anilinylethynyl)-tetraphenyl-*carbo*-benzene), hereafter denoted as Cbz is explored as photosensitizer. *Carbo*-benzenes exhibit unique properties related to the "*carbo*-aromatic" character of their C_{18} macrocyclic core: high π-electron richness (~1.7 π-e/C), persistent symmetry (*quasi-*D_{6h}), emptiness (monocycle of *ca* 8 Å diameter) and associated residual flexibility [55]. The physico-chemical properties of the di(anilin-4-ylethynyl) derivative Cbz selected for the present study are particularly adapted to its use as a redox-active photosensitizer [56]: a structural propensity for high single molecule conductance (σ ~100 nS) [57] and a high molar extinction coefficient (ε = 131 000 L mol^{-1} cm^{-1}) [55, 56] at λ_{max} = 493 nm complementary with the frequency of Ag NPs surface plasmon resonance (SPR) [58]. It is worth to notice here that the Cbz selected as photosensitizer in this work is, as most of other carbo-benzene molecules reported to date, very weakly photoluminescent, so that the possible contribution of its emission properties can be neglected in the present study [59-63].

This triptych TiO_2/Ag/Cbz photocatalyst exhibits enhanced performances under visible light and pressure (2.2 bar) compared to those of binary TiO_2/Ag and TiO_2/Cbz systems pointing to the synergy between these three components.

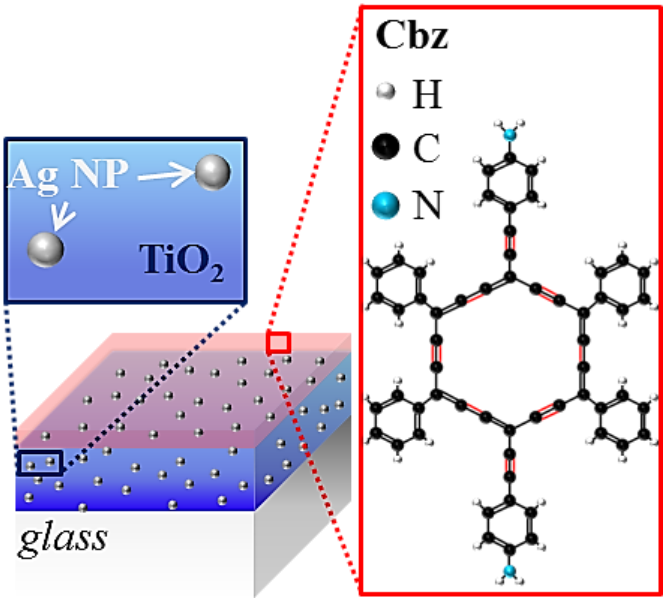

Figure 1. *Schematic hybrid triptych nanomaterial combining a TiO_2 film (blue), Ag NPs (grey spheres) and a Cbz photosensitive layer (red).*

2. Experimental Methods

All chemicals are supplied by Sigma-Aldrich. The glass wafers AF 32 are supplied by SCHOTT glass made of ideas®. Titania sols are prepared by hydrolysis of titanium alkoxide in a large excess of acidified water, according to the general procedure previously described [64] (see supporting information, Section A).

Synthesis of TiO_2/Ag/Cbz photocatalyst

TiO_2 surface. Glass or silicon substrates are cleaned by an O_2 plasma (800 W, 5 min) prior to use. 0.5 mL of TiO_2 sol is deposited on the clean substrate by spin-coating (speed: 2000 rpm, acceleration: 2000 rpm, time: 30 s). The so-obtained glass/TiO_2 samples are annealed following 2 main steps: first at 110°C for 30 min to remove the solvent and organic molecules, then at 300°C under air during 1 hour, with a heating rate of 10°C.min^{-1}, to stabilize the titanium oxide

structure. The glass/TiO_2 samples are diced into squares (1.5×1.5 cm^2) and cleaned using O_2 plasma (400 W, 5 min) prior to triptych processing.

For electron microscopy observation and spectroscopic characterization, silicon/TiO_2 samples (cleaned for 5 min with O_2 plasma at 400 W) are used.

Synthesis and deposition of Ag nanoparticles on TiO_2. The Ag nanoparticles (NPs) are grown following a previously reported procedure.[65] The TiO_2 thin film is immersed in a mixture composed by 0.5 mL of $AgNO_3$ aqueous solution ($[Ag^+] = 2.15 \times 10^{-3}$ mol/ L), 0.5 mL of sodium citrate aqueous solution ([citrate] = 0.05 mol/ L), 4.5 mL of DI water and 0.5 mL of ethanol and irradiated under UV (100 W, 2 min). The size of the nanoparticles is fixed by the irradiation duration. The samples are then annealed in air at 200°C during 30 min to ensure the grafting of Ag NPs into the TiO_2 film for a controlled localization of the plasmonic field close to the TiO_2/Ag interface. After annealing, the substrates are vigorously cleaned with DI water (~50 mL for each substrate) in order to remove all the by-products arising from the thermal decomposition of the citrate ligands. Some of these, hereafter labeled as TiO_2/Ag samples, are characterized prior to the deposition of Cbz molecules.

Synthesis and deposition of Cbz. *Para*-di(anilin-4-ylethynyl)tetraphenyl-*carbo*-benzene, a *carbo*-benzene molecule functionalized by $–NH_2$ groups (Cbz) is synthesized by a 12 step process, according to previously described procedures [56, 66]. The TiO_2/Ag substrates are immersed overnight in an anisole solution of Cbz ([Cbz] = 0.05 g/L) under stirring at 50 rpm (round-per-minute) on a shaker platform. This final step affords the triptych TiO_2/Ag/Cbz hybrid nanomaterial depicted in Figure 1.

Some of the triptych samples are prepared, first, by spin-coating the Cbz on the TiO_2 followed by the deposition of the Ag NPs with the previously described procedure. Such samples are hereafter named TiO_2/Cbz/Ag.

Materials characterization

Structural characterization of the triptych nanomaterials are performed using Scanning Electronic Microscopy (SEM) (FEI Helios 600i Nanolab) in the immersion mode at 20 kV and with a working distance of 4.2 mm. Transmission Electronic Microscopy (TEM) and High-Angle Annular Dark-Field Scanning Transmission Electronic Microscopy (HAADF-STEM) experiments are carried out in cross-section samples prepared by Focused-Ion Beam (FIB) process in a FEI Helios Nanolab. The surface of the samples is protected by a layer of sputtered carbon before the preparation of lamellas. These latter are observed on a JEM-ARM200F cold FEG at 200 kV with a probe Cs corrector reaching a spatial correction of 0.078 nm. Energy Dispersive X-ray Spectrometry (EDS) spectra are recorded using a JEOL CENTURIO SDD detector. Electron Energy Loss Spectroscopy (EELS) data are acquired using a GATAN GIF QUANTUM ER using a dispersion of 0.025 eV/channel (energy resolution of 0.3 eV), a collection semi-angle of 19.4 mrad and a convergence semi-angle of 15 mrad. Crystalline phases are detected using Grazing Incidence X-Ray Diffraction (GI –XRD, Bruker D8 Discover system) with a Cu k-alpha radiation as the source. For GI-XRD, the grazing angle is set to 1.2° and two-theta collection angle is ranged from 20° to 80° with a step of 0.05° and a dwell time of 0.1 s per point. The absence of Ag reflections for the diptych TiO_2/Ag and triptych TiO_2/Ag/Cbz samples is presumably correlated to the low content of silver on the TiO_2 thin film and the small dimensions of the samples. Note that the GI-XRD of the TiO_2 thin film provided in the supporting information is recorded from a whole silicon/TiO_2 wafer. The TiO_2 roughness and density are both characterized by Grazing Incidence X-Ray Reflectometry (GI-XRR, Bruker D8 Discover system): the grazing angle is set to 1.2° and two theta-omega collection angles is ranged from 0.4° to 3.0° with a 0.005° step and a dwell time of 0.1 s per point in all cases. X-ray

photoelectron spectroscopy (XPS) (ESCALAB 250 X-Ray photoelectron spectrometer) with a monochromatized Al-Kα radiation, a concentric hemispherical electron energy analyzer under vacuum (10^{-9} mbar) and a pass energy of 23.5 eV is used to characterize the chemical species at the interfaces of the triptych nanomaterial. The Raman scattering spectra are acquired using a Horiba-Jobin-Yvon XPlora set-up. The spectra are excited by a 532 nm laser beam focused onto the sample using a 100 × objectives (0.8 NA). The laser power intensity is kept as low as 0.1 mW in order to avoid sample heating and degradation of the organic Cbz layer. The absorbance spectra are recorded in the transmission mode from the triptych nanomaterials deposited on the transparent glass substrates using a Perkin-Elmer Lambda 950 UV-vis spectrometer equipped with an integration sphere (specular mode). The hydrophobicity of the Cbz layer is characterized by drop contact angle measurements using a Digidrop system. For each sample, three successive measurements are performed in order to check the reproducibility and estimate a mean value of the contact angle. Inductively coupled plasma - optical emission spectrometry (ICP-OES) measurements are performed at the "Service d'analyse élémentaire" of LCC-CNRS in Toulouse using a Thermo Scientific iCAP 6300 DUO spectrometer with a 3-channel, 12-roller pump and a 27.12 MHz solid state RF plasma generator. Typically, all the 10 mL (aqueous solution) involved in the photocatalytic experiments are evaporated overnight in a 50 mL Teflon tube. Concentrated nitric acid is added in the resulting mixture and then diluted in a 10 mL volumetric flask. The resulting solution (5 mL) is introduced during the ICP-OES analysis. Note that the calibration curve are realized by successive dilution of a 1000 ppm standard to give a series of standards with values at: 0.5; 1; 2; 5; 10 and 20 ppm. Each standard is analyzed in 3 replicates. The values of the working wavelength are 328.068 and 338.289 nm.

Measurement of Photocatalytic Activity

Lab-made quartz reactors are used to characterize the photocatalytic properties of the prepared samples (Figure S1). The hydrogen production is measured by gas chromatography (GC, Perkin-Elmer Clarus 580, thermal conductivity detector, PlotQ column (30 m) and PE-molisieve column (30 m), argon carrier gas). The samples (1.5 cm × 1.5 cm, 2.25 cm^2) are immersed into a 65:35 deionized water:ethanol mixture (10 mL). The quartz reactor is purged and pressurized at 2.2 bar under argon gas in order to remove the air. The samples are then irradiated with a Xenon lamp supplied by Cermax® (elliptical PE300B-10F, UV-visible, 300 W, wavelengths range from 300 nm to 1100 nm, sample placed at a distance of ~12 cm which corresponds to an optical irradiance at the sample of 28 $mW.cm^{-2}$) during 48 h and the quantity of exhausted hydrogen is measured every 6 h. For each sample, several characterization are made to ensure reproducibility of the measurements. The relative spectral distribution of the Xenon lamp is presented in Figure S2.

3. Results

Structural and chemical characterization of the triptych material

Figure 2 gives optical (a) and SEM (b) images and a TEM cross-section view (c) of a TiO_2/Ag/Cbz sample on silicon showing a uniform and dense Ag NP deposition, which are covered by a 6 nm-thick layer of Cbz. A closer examination shows that the Ag NPs (mean size: 7 ± 2 nm, areal NP density: 349 ± 10 NPs/µm²) have grown not only on the TiO_2 surface but also in the grain interstices of the TiO_2 film, as revealed by the STEM-EDS chemical profile (Figure 2d). Silver nanocrystals exhibit typical (111) crystallographic planes (blue frame in Figure 2c) [67]. The thickness, density and roughness of the TiO_2 film are estimated by GI-XRR at ~80 nm, 2.9 ± 0.01 $g.cm^{-3}$, well below the bulk density of 3.89 $g.cm^{-3}$ and ~ 2 ± 0.1 nm, respectively [68]. The

anatase single phase and the stoichiometry of the TiO_2 film are confirmed by the XRD patterns and XPS analysis, respectively. The latter gives the binding energies of the Ti $2p_{1/2}$, Ti $2p_{3/2}$ and O 1s core levels at 464.5 ± 0.1 eV, 458.8 ± 0.1 eV and 530.0 ± 0.1 eV, respectively (see supporting information, Section B-1) [69].

The Cbz layer is visible (Figure 2c) as the well-defined black contrast on top of the Ag NPs; the grey region on top of the Cbz layer is attributed to the carbon layer used to prepare the FIB lamella. EELS analyses of this top layer (Figure 2e) shows a shift from 24.3 eV to 22.4 eV in the carbon plasmon ($\sigma + \pi$) peak energy across the C-Cbz interfacial region. Laffont *et al.* reported a correlation between the plasmon ($\sigma + \pi$) energy E_p and the physical properties (resistivity, Young's modulus and thermal conductivity) of carbon species, i.e. a correlation between a shift of E_p and the nature of the carbon material [70]. Similarly, Longo *et al.* reported a shift of E_p from 33 to 28 eV when comparing diamond carbon and amorphous carbon [71, 72]. As shown in Figure 2e, both the contrast and shift of the C EELS peak reveal the information of a ~6 nm-thick Cbz layer covering the entire surface of the Ag NPs.

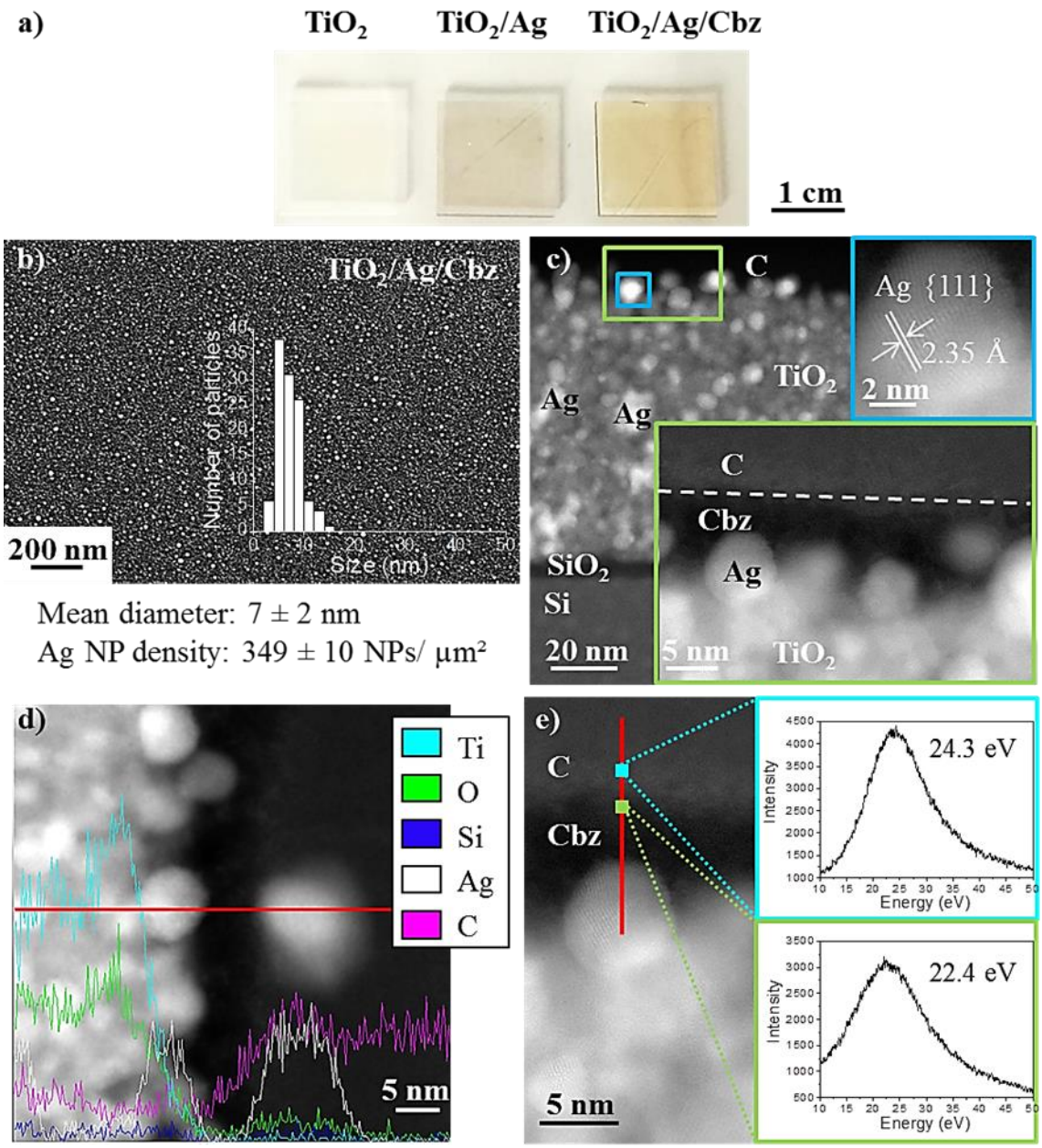

Figure 2. *a) Optical images and b) SEM observation (inset of the size distribution of Ag NPs onto the TiO_2 surface) of the TiO_2/Ag/Cbz material; c) HAADF-STEM cross-section images of TiO_2/Ag/Cbz coated with a thin sputtered carbon layer (inset of magnified images, green and blue frames); d) HAADF-STEM image and EDS spectra obtained along the red line; e) HAADF-STEM and EELS spectra: plasmon spectra from the protective carbon layer (blue square and frame) and from the Cbz layer (green square and frame). Dotted lines are eye guides.*

The Raman spectra of the triptych TiO_2/Ag/Cbz nanomaterial measured in the 400-4000 cm^{-1} range are presented in Figure 3a. Sharp peaks are clearly observed in this spectral range owing to the Surface Enhanced Raman Scattering (SERS) effect produced by the Ag NPs. Indeed, SERS effect is here observable because the Raman excitation line (532 nm) is close to the surface plasmon resonances of the aggregated Ag NPs. As a matter of fact, the Raman spectra measured from the TiO_2/Cbz substrate, i.e. without any Ag NP, reveal almost no Raman signal (black trace, Figure 3a) [73, 74].

It is worth mentioning that the weak signal/noise ratio of the SERS spectra shown in Figure 3a (red trace) is due to the fact that the Raman scattering was excited with a minimum laser power (0.1 mW) to avoid degradation of the Cbz layer which occurs at higher power because of heating resulting from the optical absorption by the Cbz and in the Ag NPs.

By comparison of these Raman spectra with the infrared spectra of Cbz and analogous *para*-dianilinyltetraphenyl-*carbo*-benzene without *exo*-macrocyclic C≡C spacers, named Cbz* (Figure S5), the main sharp modes can be unambiguously assigned to $–N(–H)_2$ (3250 and 3053 cm^{-1}), C≡C (2149 cm^{-1} and 2037 cm^{-1}) and aromatic C=C (1580 and 1511 cm^{-1}) stretching modes. According to a combined experimental and density functional theory (DFT) computational study of the Raman spectra of a series of *carbo*-benzenes [75], the two bands at 2149 cm^{-1} and 2037 cm^{-1} can be assigned to the coupled vibrations of the *exo*- and *endo*-macrocyclic C≡C bonds together. The most intense one, at 2037 cm^{-1}, corresponds to the asymmetric mode, the other (at 2149 cm^{-1}) corresponding to the superimposition of the in-phase and out-of-phase modes of the *exo*-C≡C bonds with respect to the totally symmetric vibration of the *endo*-C≡C bonds [75].

Remarkably, the intensity of band at 2149 cm^{-1} is much weaker than that at 2037 cm^{-1} when the Cbz layer is formed directly on the TiO_2 surface, which suggests a selective enhancement of

SERS intensity of both the *exo*- and *endo*- macrocyclic C≡C modes in the TiO_2/Ag/Cbz nanomaterial (Figure S6). Moreover, the enhancement of the Raman intensity of the C≡C and of the NH_2 modes in the triptych nanomaterial, indicates that the anilin-4-ylethynyl functions are localized in the close vicinity of the Ag NPs [73, 74], which suggests that the Cbz molecules are bound to the Ag NPs by the NH_2 groups.

Raman spectroscopy also reveals microstructure features, as well as the presence of electronic interactions in the diptych TiO_2/Ag and triptych TiO_2/Ag/Cbz materials. By increasing the time of the Ag NP growth, these phenomena are even more evident in the TiO_2/Ag* series with larger Ag NPs (Figure 3b, see supporting information, Section B-3) compared to the TiO_2/Ag series (see supporting information, Section B-4). The low-frequency (100-400 cm^{-1}) Raman spectra (Figure 3b) exhibit a peak characteristic of the E_g1 phonon mode of anatase TiO_2: it is located at 140 cm^{-1} in TiO_2, at 147 cm^{-1} in both TiO_2/Ag* and TiO_2/Ag*/Cbz (Figure 3b) and at 140 cm^{-1} again in the reversed triptych TiO_2/Cbz/Ag*, without TiO_2/Ag interface.

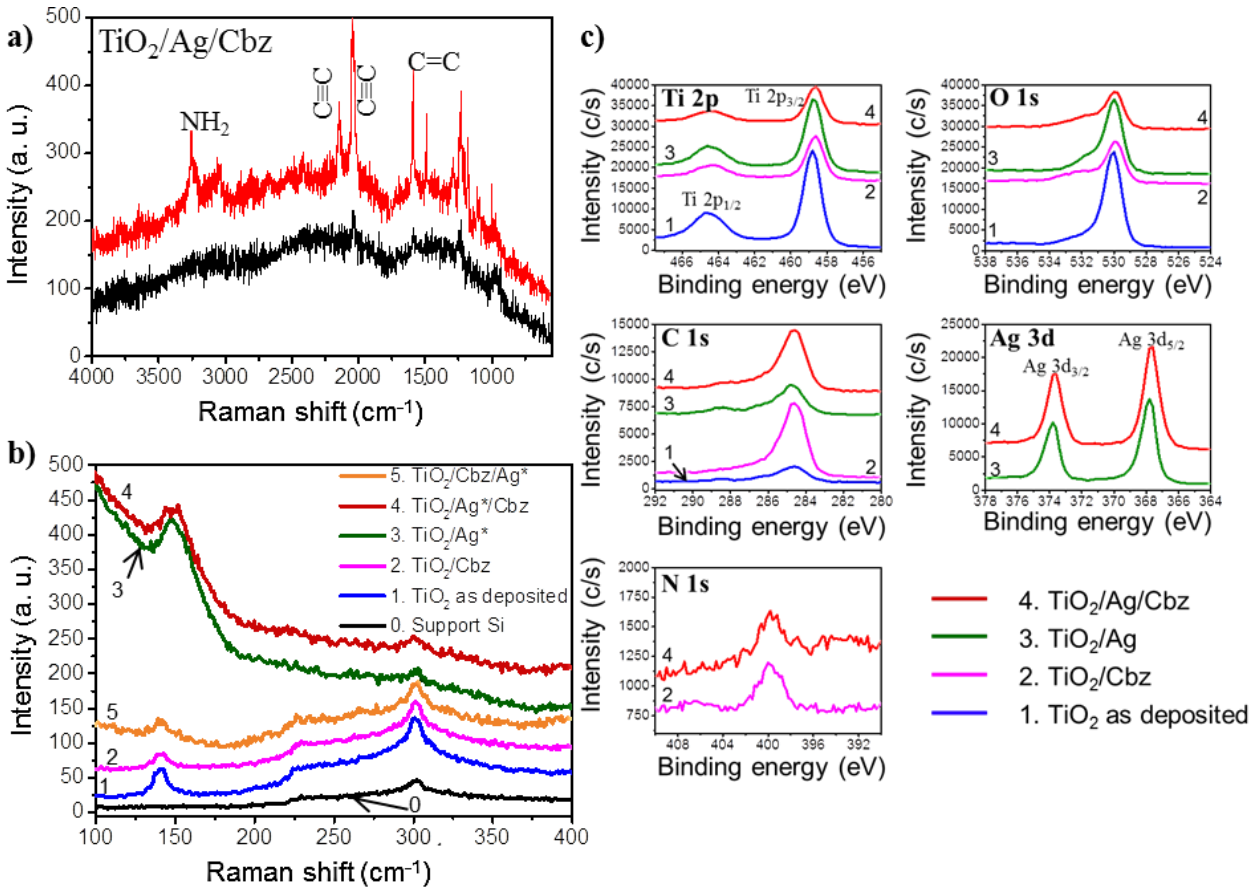

Figure 3. *a) Raman spectra of TiO_2/Ag/Cbz in the 4000-400 cm^{-1} range recorded on a single Ag aggregate (red top curve) and away from the aggregate (black bottom curve); the size of the aggregate is comparable to the laser spot size (1 µm²); b) Raman spectra recorded in the 400-100 cm^{-1} range for the Si reference substrate (0, black), TiO_2 thin film as deposited (1, blue), TiO_2/Cbz (2, violet), TiO_2/Ag* (3, dark green), TiO_2/Ag*/Cbz (4, dark red) and TiO_2/Cbz/Ag* material (5, dark orange) in the case of larger Ag NPs; c) XPS spectra of TiO_2 thin film (1, blue), TiO_2/Cbz (2, violet), TiO_2/Ag (3, green) and TiO_2/Ag/Cbz (4, red) for the Ti $2p_{3/2,1/2}$; O 1s; C 1s; Ag $3d_{5/2,3/2}$; and N 1s regions. Dotted lines are eye guides.*

Moreover, the intensity of the TiO_2 Raman peak is clearly enhanced in TiO_2/Ag and TiO_2/Ag/Cbz with respect to TiO_2 and TiO_2/Cbz/Ag. This clearly shows that the blue shift and

the intensity of the TiO_2 Raman peak correlate with the formation of the TiO_2/Ag interface. The observation of such a blue shift has already been reported in TiO_2/Au films and was attributed to the deposition of Au NPs preferably on oxygen vacancies and edge sites which favors the charge transfer interactions between TiO_2 and metal nanoparticles [13]. The charge transfer phenomenon may also enhance the photocatalytic activity since the photo-generated electron-hole pairs could be spatially separated and hence their lifetime significantly increased [76]. The blue shifted Raman peak of the TiO_2 phonon also means that the Ti-O bond is stronger at the TiO_2/Ag interface than in bulk TiO_2, revealing a charge transfer from the metal nanoparticle to the semiconductor. Moreover, the blue shift of the *Eg*1 phonon mode can also result from the mechanical constraints applied in the TiO_2 network, confirming the complete filling of the TiO_2 pores by larger Ag NPs as discussed above. These interactions are expected since the annealing step performed after NP growth, should increase the intimacy and accommodate a transition between both TiO_2 and Ag crystalline networks. Note that no significant shift is observed in the Raman spectra when the Cbz is deposited on TiO_2, pointing to the non-destructive interactions between the TiO_2 and the Cbz (violet trace, Figure 3b).

Additionally, XPS spectra given in Figure 3c clearly show an increase of the intensity of C 1s peaks and a decrease of the intensity of Ti 2p and O 1s peaks for the diptych TiO_2/Cbz and triptych TiO_2/Ag/Cbz nanomaterials which is expected when the Cbz layer covers the top surface (see supporting information, Section B-5). Finally, XPS spectra also show that N 1s core level (from -NH_2 groups) is exactly at the same position (399.8 eV) than for TiO_2/Cbz which suggests a similar binding between Cbz and TiO_2 and the Ag NP surfaces (Figure 3c, see supporting information, Section B-5). Note that some carbon contamination coming from atmospheric adsorbed carbon species is detected on a few samples (without a coating of Cbz) with a C 1s peak of weak intensity (Figure 3c).

UV-visible spectroscopy and hydrogen production of the diptych and triptych nanomaterials

The optical absorption spectra of the investigated samples are presented in Figure 4a,b. The contribution of each component of the diptych and triptych nanomaterials can be clearly distinguished: (i) the strong band-gap absorption of TiO_2 is observed around 280 nm; (ii) the contribution of the Ag NPs SPR is visible around 430 nm in both TiO_2/Ag and TiO_2/Ag/Cbz compared to pure TiO_2 and is consistent with the SPR wavelength expected for spherical 7 ± 2 nm Ag NPs [39, 40]; (iii) the main absorption band of Cbz molecules resulting from the overlapping of the two strongest Gouterman transitions (HOMO-1/HOMO → LUMO/LUMO+1) appears around 494 nm as a shoulder in the TiO_2/Ag/Cbz spectrum and is probably enhanced by the SPR of the Ag NPs [59, 60, 77, 78]. Note that in the reversed triptych system TiO_2/Cbz/Ag, the Ag NPs are no longer in direct contact with the TiO_2 surface, which affects their LSPR properties by red-shifting and broadening [79], resulting in an overlap of the Ag NPs LSPR peak with the absorption band of Cbz, leading to the observation of only one broad absorption band (Figure 4b). From these UV-visible analyses, the band gap of the TiO_2 thin films has been calculated for the different diptych and triptych systems and are found both close to ~3.4 eV (Figure S14).

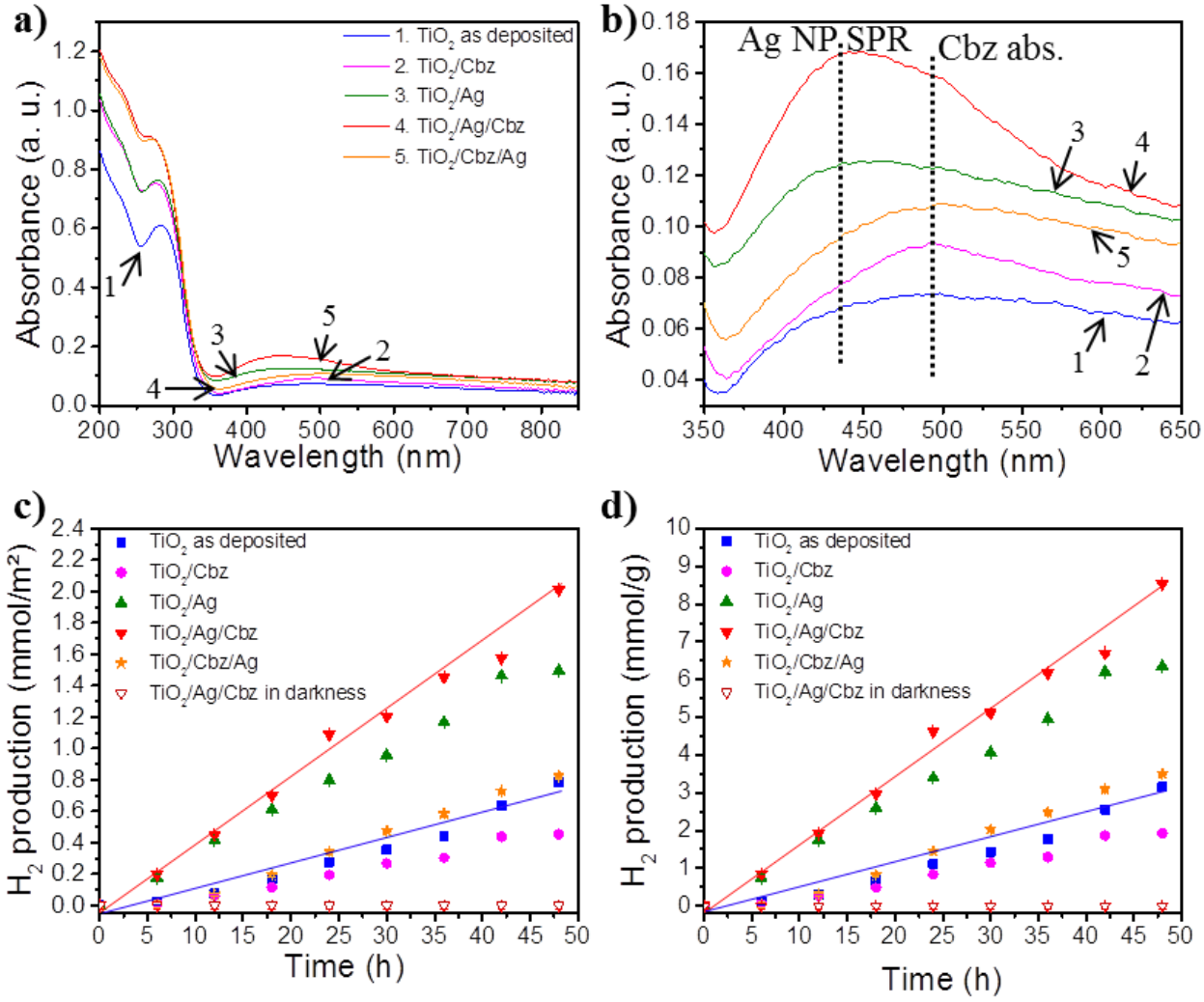

Figure 4. *a) UV-visible spectra (in transmission) in the 200-850 nm region and; b) in the 350-650 nm region; c) H_2 production per surface units and; d) per mass units for pure ~80 nm TiO_2 thin film (1, blue, square), TiO_2/Cbz (2, violet, circle), TiO_2/Ag (3, green, triangle), TiO_2/Ag/Cbz (4, red, reverse triangle) and TiO_2/Cbz/Ag (5, orange, star) on glass substrates (1.5 × 1.5 cm) immersed into a 65:35 deionized water:ethanol solution at room temperature and pressurized under argon at 2.2 bar. Error scale bars of hydrogen quantity are added for each plot. Note that the monitoring of the H_2 production in darkness is for the triptych TiO_2/Ag/Cbz material (red, empty reverse triangle) in the same conditions: deionized 65:35 water:ethanol solution at room temperature under argon at 2.2 bar.*

The H_2 production is measured by immersing the 2.25 cm² samples into 10 mL of a 35% aqueous ethanol solution in a hand-made quartz reactor. Importantly, the reactor is purged and pressurized with 2.2 bar of argon gas before analyses and is not placed under vacuum as it is the case in many literature reports.[11, 80] A sample of bare TiO_2 thin film is also studied as a reference.

The hydrogen production of all tested samples (Figure 4c,d) increases linearly during the two days tests and reveals a stable catalytic performance during 48 hours. The measured hydrogen production rates are determined: 0.03 $mmol.m^{-2}.h^{-1}$ (0.13 $mmol.g^{-1}.h^{-1}$) and 0.04 $mmol.m^{-2}.h^{-1}$ (0.18 $mmol.g^{-1}.h^{-1}$) for the diptych TiO_2/Ag and triptych TiO_2/Ag/Cbz nanomaterials, respectively. These rates exceed by more than a factor 2 those of the TiO_2 reference layer: 0.02 $mmol.m^{-2}.h^{-1}$ (0.06 $mmol.g^{-1}.h^{-1}$), of the TiO_2/Cbz: 0.009 $mmol.m^{-2}.h^{-1}$ (0.04 $mmol.g^{-1}.h^{-1}$) and of the reversed triptych TiO_2/Cbz/Ag nanomaterial: 0.02 $mmol.m^{-2}.h^{-1}$ (0.07 $mmol.g^{-1}.h^{-1}$), hence underlying the synergetic role of the TiO_2/Ag in the PC process (Figure 4c,d, Figure 5). Moreover, the production rate of the triptych TiO_2/Ag/Cbz is larger than that of the diptych TiO_2/Ag by ~33% which gives an estimate of the contribution of the Cbz photo-sensitizer to the photocatalytic process.

The extension of the TiO_2/Ag/Cbz triptych absorption over a large visible range (from 400 to 600 nm) as compared to TiO_2 alone may lead to a more efficient utilization of the visible light and thus enhance the hydrogen production. Furthermore, because the absorptions of Ag NPs (SPR) and Cbz (maximum absorption band) take place at two different wavelengths, their combination can also induce the observed enhancement of the photocatalytic efficiency.

4. Discussion

Influence of the respective spatial distribution of the three components

To better assess the respective role of the Cbz organic dye and plasmonic Ag NPs into the TiO_2/Ag/Cbz nanomaterial, three different samples are assembled: (1) a sample without the organic dye: TiO_2/Ag; (2) a sample without Ag NPs: TiO_2/Cbz; (3) a sample where the Cbz layer is deposited before the growth of the Ag NPs i.e. preventing the contact between the TiO_2 pores and the environing medium: the reversed triptych: TiO_2/Cbz/Ag. In the latter sample, no shift of the phonon mode E_g1 is measured (Figure 3b, Figure S10) indicating the absence of mechanical constraint on the TiO_2 lattice, as expected: the Cbz layer indeed covers the surface of the TiO_2 film and avoid the embedding of Ag NPs in the pores of the metal oxide film.

The samples are placed under Ar flow and irradiated in the presence of ethanol in the same conditions as those used for the TiO_2/Ag/Cbz nanomaterial. In all the cases, the hydrogen production increases linearly over the 48 h (Figure 4c,d). The hydrogen production rate for each sample is represented in Figure 5. As expected, the TiO_2/Ag substrate is more efficient than the pure TiO_2 thin film due to SPR effects, but the hydrogen production rate of this diptych is lower than that of the TiO_2/Ag/Cbz triptych.

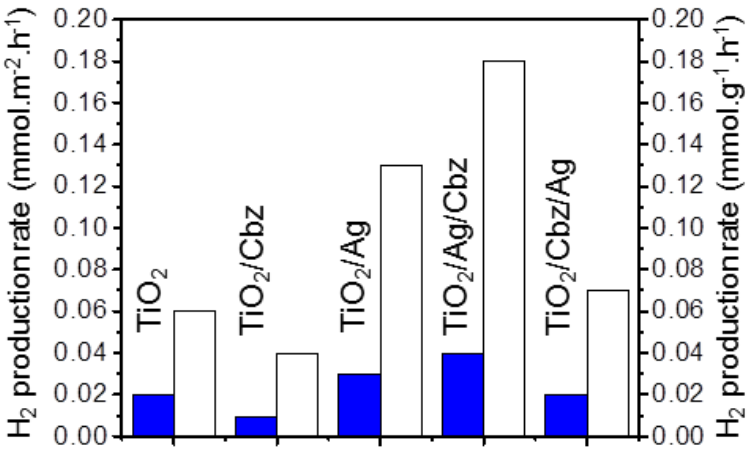

Figure 5. *The H_2 production rate per surface units (blue) and per gram (white) for the tested photocatalysts.*

The diptych TiO_2/Ag nanomaterial is 1.9 times more efficient than pure TiO_2 if the H_2 production rate is expressed per m² (0.03 $mmol.m^{-2}.h^{-1}$), and 2.2 times more efficient (0.13 $mmol.g^{-1}.h^{-1}$), if this rate is expressed per gram. For the TiO_2/Ag/Cbz triptych, a slight improvement of the production rate is observed, up to 2 times (0.04 $mmol.m^{-2}.h^{-1}$), or up to 3 times more (0.18 $mmol.g^{-1}.h^{-1}$) than pure TiO_2 depending on the considered unit (Figure 5). In contrast, the decreased efficiency observed for the TiO_2/Cbz diptych clearly evidences a synergistic effect between the three components in the TiO_2/Ag/Cbz triptych.

Additionally, the stability of the TiO_2/Ag/Cbz triptych is tested by cyclic photocatalytic H_2 production monitoring (Figure 6). After 5 cycles, no significant decay in the photocatalytic activity is observed, suggesting that TiO_2/Ag/Cbz have good stability in photocatalytic H_2 production under harsh environment: simulated sunlight illumination (optical irradiance at the sample of 28 $mW.cm^{-2}$), room temperature and pressure (2.2 bar). The optical and SEM observations of the samples after the photocatalytic experiments show a better stability of the TiO_2/Ag/Cbz triptych compared to the TiO_2/Ag diptych on which the photoactive film is highly

degraded (Figure S17). These observations reveal that the Cbz layer also acts as a protective layer against the TiO_2 photocorrosion [81, 82].

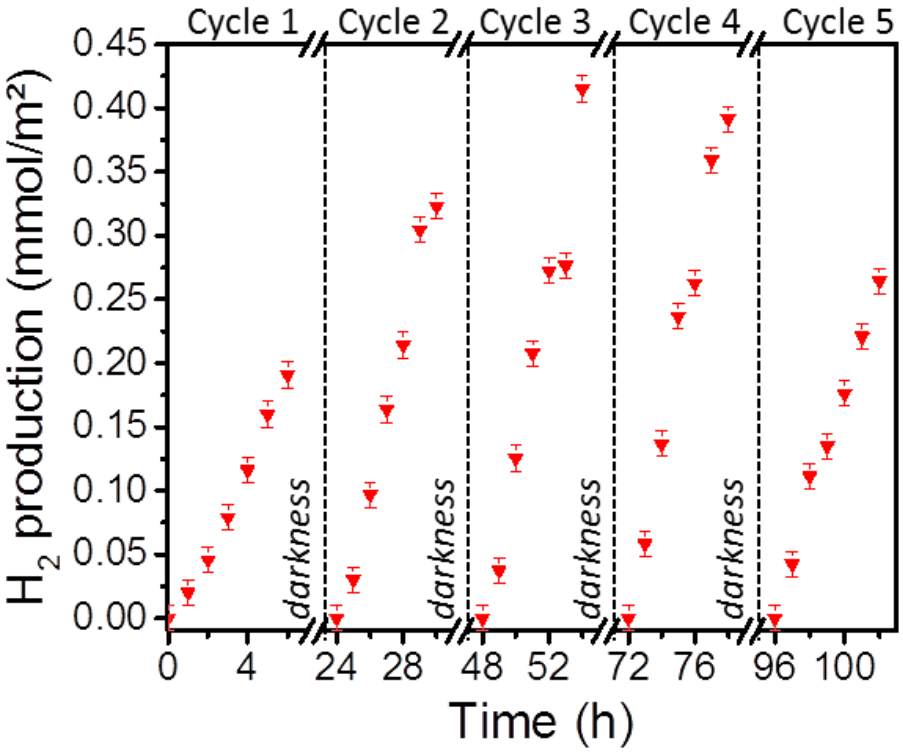

Figure 6. *Cyclability of TiO_2/Ag/Cbz triptych in H_2 production under visible light irradiation. Cumulated evolution of hydrogen from a triptych sample (1 × 1 cm) immersed into a 65:35 deionized water:ethanol solution at room temperature and pressurized under argon at 2.2 bar. Error scale bars of hydrogen quantity are added for each plot. Note that each cycle is realized over 6 h after a period of 18 h into darkness (i.e. the sample remains immersed into the deionized 65:35 water:ethanol solution under pressure of argon (2.2 bar) and at room temperature during the 18 h of darkness).*

This remarkable enhancement of the hydrogen production rate observed with TiO_2/Ag/Cbz and to a lesser extent with TiO_2/Ag is attributed to the Ag metal link in the effective vertical

Schottky junction between Ag NPs and TiO_2. The plasmon mode corresponds to discrete states (interbands 4d – 5s) of coupling between the incident light and the electronic density oscillation within the Ag NPs. The energy of the photon is transferred to electrons which can get over the Shottky barrier at the interface between TiO_2 and Ag and be injected into the conduction band of TiO_2. This mechanism called plasmon induced electron transfer from metallic particles to a TiO_2 film is schematically represented in Figure 7. Importantly, the surface plasmon resonance of the Ag NPs spectral domain is overlapping with the optical absorption of the Cbz molecules, the latter giving a shoulder of the Ag NPs LSPR broad band (Figure 4b): this leads to a plasmonic enhancement of the photo-generation of electrons and holes and might explain the synergy observed in the hydrogen production with the triptych nanomaterials.

The lower hydrogen production activity of the reversed TiO_2/Cbz/Ag triptych, close to the TiO_2/Cbz level, can be tentatively explained by two effects. Ag NPs absorb light, but without the metal-link between Ag and TiO_2, hot electrons cannot be transferred into the TiO_2 thus preventing the enhancement of hydrogen production. Nevertheless the energy is transferred to the Cbz dye which contributes to slightly increase the hydrogen production as compared to TiO_2/Cbz [83], and thus probably because of the electron transport ability of the Cbz molecule [57]. The poor performance of the latter sample as compared to pure TiO_2 could be attributed to the hydrophobicity of the Cbz layer, hampering the interaction between the TiO_2 surface and water molecules.

Indeed, the contact angles systematically increases when the Cbz layer is deposited on the samples as compared to those measured for the same materials without organic layer (see supporting information, Section B-8). For example, the contact angle of 62 ± 3° of the TiO_2/Ag diptych increases up to 100.2 ± 0.1° after deposition of the Cbz layer. The fact that the triptych system, despite the screening of charge in addition to the physico-chemical separation of water

molecules from the catalytic surface sites, which is clearly visible from the diptych response, is a clear illustration of the synergy between Ag nanoparticles and Cbz molecules. With this respect, a better control of the Cbz layer thickness, as well as its organization at the molecular level, to facilitate water diffusion, is a potential source of enhancement of the triptych material performances.

All these observations clearly evidence the synergetic effect of the three components in the triptych materials and highlight the key role of electron transfer mechanisms for the H_2 production as illustrated in Figure 7.

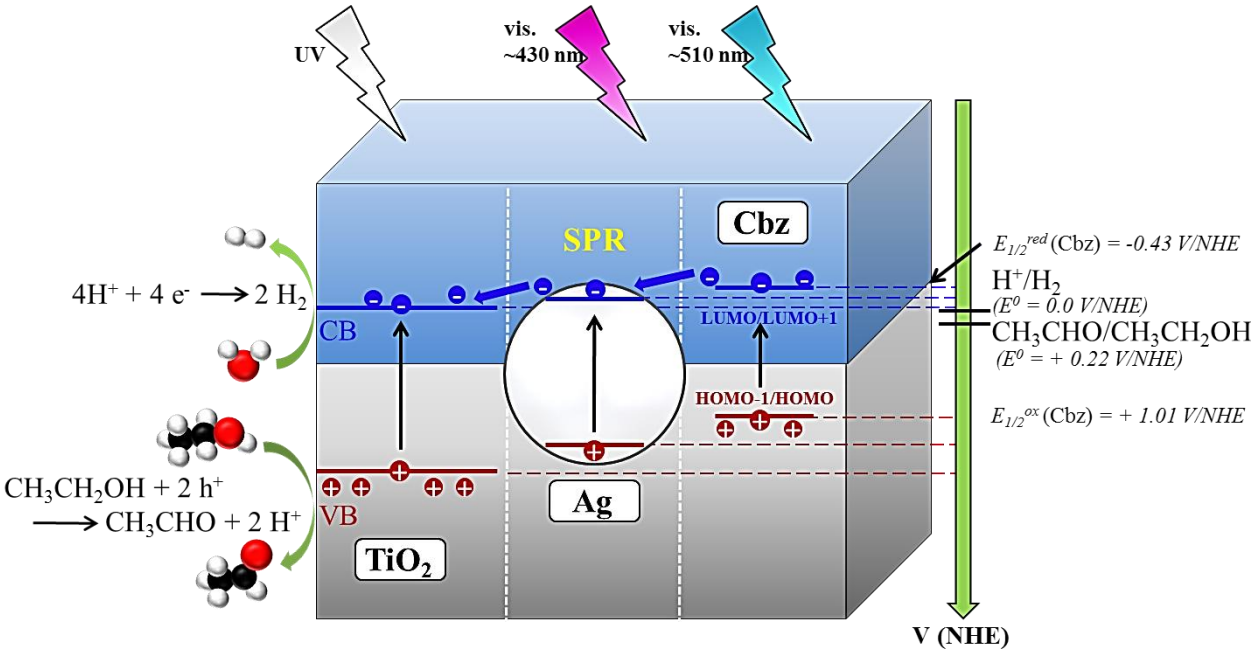

Figure 7. *Illustration of a possible electron transfer mechanism in the triptych TiO_2/Ag/Cbz material. The semiconductor thin film (TiO_2), the photosensitive Cbz layer and Ag nanoparticle are depicted as grey, blue and white, respectively. Note that for each component of the triptych, the band diagram is also depicted.*

Influence of the Ag loading and size

As the Ag-TiO_2 metal link was shown to play a crucial role in the hydrogen production performances of the TiO_2/Ag/Cbz nanomaterial, this last section addresses the effect of loading and size of Ag NPs. The porosity of the TiO_2 films allows nucleation and growth of Ag NPs inside the pores, from molecular precursors such as $AgNO_3$, which has a larger Van der Waals size than water or ethanol molecules. The size of Ag NPs can be easily tuned by modifying the time of irradiation inducing the process of photo-deposition of Ag NPs from their salt precursor. Typically, the lengthening of the UV irradiation time for the photo-reduction process from 2 to 30 min induces an increase of the size of the Ag NPs in the corresponding TiO_2/Ag* series. Two populations of Ag NPs are observed after a 30 min illumination: well-defined small particles with an average diameter of 18 ± 6 nm and larger ones with an average diameter of 30 ± 2 nm, the areal density being almost constant at ~ 344 ± 10 NPs/ µm² (see supporting information, Section B-3). Inside the pores of the TiO_2 film, the Ag NPs growth is limited by the volume of the pores, thus leading to the first population of smaller Ag NPs (18 ± 6 nm), while the larger NPs (30 ± 2 nm) are those located at the TiO_2 film surface where their growth is not limited by any confinement. The smaller Ag NPs are thus the result of the growth inside the pores, whereas the bigger particles are those which grew on the TiO_2 surface.

The TiO_2/Ag* diptych produces much less hydrogen than TiO_2/Ag: 0.004 $mmol.m^{-2}.h^{-1}$ (0.02 $mmol.g^{-1}.h^{-1}$) and 0.03 $mmol.m^{-2}.h^{-1}$ (0.13 $mmol.g^{-1}.h^{-1}$), respectively (see supporting information, Section B-7). Three explanations can be proposed: (1) the aggregation of Ag NPs decreases the number and the accessibility of the active sites on the surface of the triptych material; (2) a too large covering of the surface by silver can shield the UV light absorption by the TiO_2, and thus decrease the utilizing efficiency of photoelectrons [84]; (3) the reduction of free TiO_2 surface accessible to water molecules since the pores are filled with ~18 nm plasmonic particles (Figure

S9). The SPR effect of 18 nm Ag NPs completely embedded into the TiO_2 pores is characterized at ~380 nm (see supporting information, Figure S13) [85]. The maximum of the SPR absorption band resulting from the contribution of two Ag NP populations onto the surface (18 ± 6 nm and 30 ± 2 nm, Figure S8b) in TiO_2/Ag* remains at ~430 nm, i.e. roughly at the same position as for ~7 nm Ag NPs obtained after a 2 min irradiation process. In the dual population case, we believe the largely predominant population (18 nm) to be responsible for the non-shifted TiO_2/Ag* result (no shifting expected for NPs with diameter < ~20 nm), the population with larger diameter being minor, with a contribution also vanishing due to the broadening of the overall absorption peak. So, the size of the Ag NPs has apparently no effect on the efficiency of the water reduction photocatalyst. However, a higher loading of NPs appears to be critical on the photocatalyst performances since it reduces the TiO_2 effective surface area in the final material.

Comparison with already published catalytic materials

Finally, the main characteristic and PC-WS performances of our TiO_2/Ag/Cbz photocatalyst are reported in Table 1, together with other triptych materials (mostly in nanopowder form) described in the recent literature[52, 86-89]. Note that the comparison is difficult because the experimental parameters are highly variable. We characterize the H_2 production under 2.2 bar representative of practical applications whereas a major part of published works [11, 80] measure the photocatalytic activity in a quartz reactor under vacuum, which is highly favorable to hydrogen production because of the shift of the chemical equilibrium according to the Le Chatelier's principle: $2\ H_2O = 2\ H_2 + O_2$. Nevertheless, our TiO_2/Ag/Cbz photocatalyst thin film exhibits very good PC-WS performance (180 $\mu mol.g^{-1}.h^{-1}$) under high pressure (2.2 bar). In addition, compared to other works, the manufacturing process is not only low costs but also

provides robust material against photocorrosion compared to nanopowders (established over 48h (see supporting information, Figure S17 and Section B-13)).

Table 1 - PC performance of different type of triptych photocatalysts under visible light irradiation.

Material		Surface area	Solution Composition	Light Intensity (mW/cm^2)	Light Source (Spectrum Light source)	H_2 Production Rate ($\mu mol.g^{-1}.h^{-1}$)	Pressure (bar)	Cost	Robustness	Reference
nanopowder	Au@r-GO/TiO2	122.9 $m^2.g^{-1}$	75% H_2O 25% MeOH	100 $mW.cm^{-2}$	Xenon light source ($\lambda > 400$ nm)	300 $\mu mol.g^{-1}.h^{-1}$	1 bar	$$$	-	[86]
nanopowder	Au/TiO_2-gC_3N_4	75 $m^2.g^{-1}$	99% H_2O 1% MeOH	12.5 $mW.cm^{-2}$	150-W metal halide lamp (λ: all spectrum)	580 $\mu mol.g^{-1}.h^{-1}$	-	$$$	-	[52]
nanopowder	Ag-TiO_2-graphene	-	80% H_2O 20% MeOH	450.1 $mW.cm^{-2}$	300-W Xenon lamp (λ: all spectrum)	130 $\mu mol.g^{-1}.h^{-1}$	1 bar	$$	-	[87]
nanosheet	TiO_2-Pt-rGO	334.7 $m^2.g^{-1}$	90% H_2O 10% MeOH	-	300-W Xenon lamp (λ: all spectrum)	4000 $\mu mol.g^{-1}.h^{-1}$	1 bar	$$	-	[89]
nanosheet	TiO_2-Ag-rGO	70.83 $m^2.g^{-1}$	80% H_2O 20% MeOH	-	280-W Xenon lamp (λ: all spectrum)	593 $\mu mol.g^{-1}.h^{-1}$	-	$$	-	[88]
thin film	TiO_2/Ag/Cbz	4.25 $m^2.g^{-1}$ (*)	65% H_2O 35% EtOH	28 $mW.cm^{-2}$	300-W Xenon lamp (λ: 300-1100 nm)	180 $\mu mol.g^{-1}.h^{-1}$ 40 $\mu mol.m^{-2}.h^{-1}$	2.2 bar	$	✓✓✓	This work

(*)Note that the surface area of TiO_2/Ag/Cbz is calculated from the dimension and mass of the thin film since the surface area is too weak to be measured by Brunauer-Emmett-Teller (BET) method.

5. Conclusion

In summary, the innovative TiO_2/Ag/Cbz triptych system with an ultralow weight of photocatalyst, which is of paramount importance in the perspective of low-cost applications in the field of energy, benefits from synergy effect for hydrogen production by pure photocatalysis as shown by comparison with the diptych systems. The relevance of triptych materials for WS involving a semiconductor thin film, a plasmonic nanoparticle and a specific photosensitive molecule of the *carbo*-benzene genus is established. Thanks to an adapted procedure of photo-

deposition, the pores of a TiO_2 thin film can be metallized by silver nanoparticles in one step. The present work not only demonstrates the high interest of *carbo*-benzene molecules in green hydrogen production applications, but also provides a mechanistic insight highlighting two key requirements: the need for a Schottky junction between silver and TiO_2 and the precise localization of the dye in triptych materials in order to promote a synergic effect for H_2 production by hydrogen evolution reaction.

Furthermore, although thin films-based systems are typically used in photoelectrochemical processes for hydrogen production, the improvement of thin films efficiency by their combination with adequate materials like plasmonic nanoparticles and/or photosensitive and innovative molecules was demonstrated, allowing their use in pure photocatalytic conditions i.e. without any need of electric energy to produce hydrogen from water and sunlight, and more importantly under usual conditions of ambient temperature and pressure.

Supplementary data

Supplementary material is available including detailed synthesis of TiO_2 sols; characterization of TiO_2 films; supplementar SEM, Raman, Infrared, UV-visible and XPS spectroscopies and angle contact measurements for the considered diptych and triptych materials.

Author Information

Corresponding author

Correspondence to: Jeremy Cure, jcure@laas.fr & Carole Rossi, crossi@laas.fr

Author contributions

J. C. prepared all the materials, performed all the H_2 production measurements and directed and supervised the research. K. C. performed the synthesis of the photosensitive *carbo*-benzene molecule. A. M. provided support for Raman experiments. All HAADF-STEM and TEM images were obtained by T. H. . P. A. provided the titania sol. C. T. performed XRD measurements. Y. J. C. provided support for XPS data analysis. V. M. and R. C. provided support for the synthesis of *carbo*-benzene molecules. A. E. provided support for manuscript preparation. C. R. directed and supervised the research with J. C. .

Competting financial interests

The authors declare no competting financial interests.

Acknowledgement

All the synthesis and spectroscopic characterization and modeling were supported by ANR and the Université de Toulouse (IDEX MUSE project). This work was supported by LAAS-CNRS technology platform, a member of Renatech network. Jean-François Veyan is acknowledged for his help in the measurements of the XPS spectra. The authors thank Claudie Josse and Armel Descamps-Mandine (Centre de Microcaractérisations Raimond Castaing) for the preparation of lamelas and HAADF-STEM observations, Alain Moreau for the ICP measurements and Andréa Nicollet and Séverine Vivies for their help with XRD characterization. Tercio de Freitas Paulo is deeply acknowledged for his help in the assigment of the Raman spectra.

References

[1] 10th Stakeholder Forum - Fuel Cell and Hydrogen Technology: Europe's Journey to a Greener World, Publications Office of the European Union, 2017.
[2] S. Dutta, A review on production, storage of hydrogen and its utilization as an energy resource, J. Ind. Eng. Chem. 20(4) (2014) 1148-1156.
[3] ADEME, the Role of Hydrogen in the Energy Transition, Technical review (2018) 1-15.
[4] B.A. Pinaud, J.D. Benck, L.C. Seitz, A.J. Forman, Z. Chen, T.G. Deutsch, B.D. James, K.N. Baum, G.N. Baum, S. Ardo, H. Wang, E. Miller, T.F. Jaramillo, Technical and economic feasibility of centralized facilities for solar hydrogen production via photocatalysis and photoelectrochemistry, Energy Environ. Sci. 6(7) (2013) 1983-2002.
[5] F.F. Abdi, L. Han, A.H.M. Smets, M. zeman, B. Dam, R. Van De Krol, Efficient solar water splitting by enhanced charge separation in a bismuth vanadate-silicon tandem photoelectrode, Nat. Commun. 4 (2013) 2195.
[6] J. Luo, D.A. Vermaas, D. Bi, A. Hagfeldt, W.A. Smith, M. Grätzel, Bipolar membrane-assisted solar water splitting in optimal pH, Adv. Energy Mater. 6(13) (2016) 1600100.
[7] J.W. Ager, M. Shaner, K. Walczak, I.D. Sharp, S. Ardo, Experimental demonstrations of spontaneous, solar-driven photoelectrochemical water splitting, Energy Environ. Sci. 8(10) (2015) 2811-2824.
[8] M.S. Prevot, N. Guijarro, K. Sivula, Enhancing the Performance of a Robust Sol-Gel-Processed p-Type Delafossite CuFeO2 Photocathode for Solar Water Reduction, ChemSusChem 8(8) (2015) 1359-1367.
[9] A. Fujishima, K. Honda, Electrochemical Photolysis of Water at a Semiconductor Electrode, Nature 238(5358) (1972) 37-8.
[10] T. Hisatomi, J. Kubota, K. Domen, Recent advances in semiconductors for photocatalytic and photoelectrochemical water splitting, Chem. Soc. Rev. 43(17) (2014) 7520-7535.
[11] Z. Wang, C. Li, K. Domen, Recent developments in heterogeneous photocatalysts for solar-driven overall water-splitting, Chem. Soc. Rev. 48(7) (2018) 2109-2125.
[12] K. Maeda, K. Teramura, D. Lu, T. Takata, N. Saito, Y. Inoue, K. Domen, Photocatalyst releasing hydrogen from water, Nature 440(7082) (2006) 295.
[13] A.A. Melvin, K. Illath, T. Das, T. Raja, S. Bhattacharyya, C.S. Gopinath, M-Au/TiO2 (M = Ag, Pd, and Pt) nanophotocatalyst for overall solar water splitting: role of interfaces, Nanoscale 7(32) (2015) 13477-13488.
[14] X. Wang, S. Jin, H. An, X. Wang, Z. Feng, C. Li, Relation between the photocatalytic and photoelectrocatalytic performance for the particulate semiconductor-based photoconversion systems with surface phase junction structure, J. Phys. Chem. C 119(39) (2015) 22460-22464.
[15] Y. Goto, T. Hisatomi, Q. Wang, T. Higashi, K. Ishikiriyama, T. Maeda, Y. Sakata, S. Okunaka, H. Tokudome, M. Katayama, S. Akiyama, H. Nishiyama, Y. Inoue, T. Takewaki, T. Setoyama, T. Minegishi, T. Takata, T. Yamada, K. Domen, A Particulate Photocatalyst Water-Splitting panel for Large-Scale Solar Hydrogen Generation, Joule 2(3) (2018) 509-520.
[16] A. Kudo, Y. Miseki, Heterogeneous photocatalyst materials for water splitting, Chem. Soc. Rev. 38(1) (2009) 253-278.
[17] F.E. Osterloh, Inorganic Materials as Catalysts for Photochemical Splitting of Water, Chem. Mater. 20(1) (2008) 35-54.
[18] X.B. Chen, S.H. Shen, L.J. Guo, S.S. Mao, Semiconductor-based Photocatalytic Hydrogen Generation, Chem Rev 110(11) (2010) 6503-6570.
[19] Y. Tian, T. Tatsuma, Mechanisms and applications of plasmon-induced charge separation at TiO2 films loaded with gold nanoparticles, J Am Chem Soc 127(20) (2005) 7632-7637.
[20] A. Takai, P.V. Kamat, Capture, Store, and Discharge. Shuttling Photogenerated Electrons across TiO2-Silver Interface, Acs Nano 5(9) (2011) 7369-7376.

[21] S.U.M. Khan, M. Al-Shahry, W.B. Ingler, Efficient photochemical water splitting by a chemically modified n-TiO2 2, Science 297(5590) (2002) 2243-2245.
[22] J.B. Varley, A. Janotti, C.G. Van de Walle, Mechanism of Visible-Light Photocatalysis in Nitrogen-Doped TiO2, Adv Mater 23(20) (2011) 2343-+.
[23] H.C. Rojas, S. Bellani, E.A. Sarduy, F. Fumagalli, M.T. Mayer, M. Schreier, M. Grätzel, F. Di Fonzo, M.R. Antognazza, All Solution-Processed, Hybrid Organic-Inorganic Photocathode for Hydrogen Evolution, ACS Omega 2(7) (2017) 3424-3431.
[24] E. Reisner, D.J. Powell, C. Cavazza, J.C. Fontecilla-Camps, F.A. Armstrong, Visible Light-Driven H2 Production by Hydrogenases Attached to Dye-Sensitized TiO2 Nanoparticles, J. Am. Chem. Soc. 131(51) (2009) 18457-18466.
[25] M. Watanabe, S. Sun, T. Ishihara, T. Kamimura, M. Nishimura, F. Tani, Visible Light-Driven Dye-Sensitized Photocatalytic Hydrogen Production by Porphyrin and its Cyclic Dimer and Trimer: Effect of Multi-Pyridyl-Anchoring groups on Photocatalytic Activity and Stability, ACS Appl. Energy Mater. (2018) Ahead of print.
[26] X. Zhang, Y. Sun, X. Cui, Z. Jiang, A green and facile synthesis of TiO2/graphene nanocomposites and their photocatalytic activity for hydrogen evolution, Int. J. Hydrogen Energy 37(1) (2012) 811-815.
[27] Q. Huang, S. Tian, D. Zeng, X. wang, W. Song, Y. Li, W. Xiao, C. Xie, enhanced Photocatalytic Activity of Chemically Bonded TiO2/Graphene Composites Based on the Effective Interfacial Charge Transfer through the C-Ti Bond, ACS Catal. 3(7) (2013) 1477-1485.
[28] L.K. Putri, L.L. Tan, W.J. Ong, W.S. Chang, S.P. Chai, Graphene oxide: Exploiting its unique properties toward visible-light-driven photocatalysis, Appl Mater Today 4 (2016) 9-16.
[29] S. Min, G. Lu, Dye-cosensitized graphene/Pt photocatalyst for high efficient visible light hydrogen evolution, Int. J. Hydrogen Energ. 37(14) (2012) 10564-10574.
[30] E.Z. Liu, L.M. Kang, Y.H. Yang, T. Sun, X.Y. Hu, C.J. Zhu, H.C. Liu, Q.P. Wang, X.H. Li, J. Fan, Plasmonic Ag deposited TiO2 nano-sheet film for enhanced photocatalytic hydrogen production by water splitting, Nanotechnol. 25(16) (2014) 165401.
[31] Y.C. Yin, E.Z. Liu, H. Li, J. Wan, J. Fan, X.Y. Hu, J. Li, C.N. Tang, C.C. Pu, Fabrication of plasmonic Au/TiO2 nanotube arrays with enhanced photoelectrocatalytic activities, Ceram. Int. 42(8) (2016) 9387-9395.
[32] Y. Liu, S. Yang, S. Zhang, H. Wang, H. Yu, Y. Cao, F. Peng, Design of cocatalyst loading position for photocatalytic water splitting into hydrogen in electrolyte solutions, Int. J. Hydrogen Energy 43(11) (2018) 5551-5560.
[33] S. Bai, L. Yang, C. Wang, Y. Lin, J. Lu, J. Jiang, Y. Xiong, Boosting Photocatalytic water Splitting: Interfacial Charge Polarization in Atomically Controlled Core-Shell Cocatalysts, Angew. Chem. Int. Ed. 54 (2015) 14810-14814.
[34] J. Liu, G. Liu, M. Li, W. Shen, Z. Liu, J. Wang, J. Zhao, L. Jiang, Y. Song, Enhancement of photochemical hydrogen evolution over Pt-loaded hierarchical titania photonic crystal, Energy Environ. Sci. 3(10) (2010) 1503-1506.
[35] B.D. Fraters, R. Amrollahi, G. Mul, How Pt nanoparticles affect TiO2-induced gas-phase photocatalytic oxidation reactions, J. Catal. 324 (2015) 119-126.
[36] Z. Zhang, L. Zhang, M.N. Hedhili, H. Zhang, P. Wang, Plasmonic Gold Nanocrystals Coupled with Photonic Crystal Seamlessly on TiO2 Nanotube Photoelectrodes for Efficient Visible Light Photoelectrochemical Water Splitting, Nano Lett. 13(1) (2013) 14-20.
[37] Y.-C. Pu, G. Wang, K.-D. Chang, Y. Ling, Y.-K. Lin, B.C. Fitzmorris, C.-M. Liu, X. Lu, Y. Tong, J.Z. Zhang, Y.-J. Hsu, Y. Li, Au Nanostructure-Decorated TiO2 nanowires Exhibiting Photoactivity Across Entire UV-visible Region for Photoelectrochemical Water Splitting, Nano Lett. 13(8) (2013) 3817-3823.

[38] H. Gao, P. Zhang, J. Zhao, Y. Zhang, J. Hu, G. Shao, Plasmon enhancement on photocatalytic hydrogen production over the Z-scheme photosynthetic heterojunction system, Appl. Catal. B 210 (2017) 297-305.
[39] M.-Z. Ge, C.-Y. Cao, S.-H. Li, Y.-X. Tang, L.-N. Wang, N. Qi, J.-Y. Huang, K.-Q. Zhang, S.S. Al-Deyab, Y.-K. Lai, In situ plasmonic Ag nanoparticle anchored TiO2 nanotube arrays as visible-light-driven photocatalysts for enhanced water splitting, Nanoscale 8(9) (2016) 5226-5234.
[40] A. Sreedhar, T.V.M. Sreekanth, J.H. Kwon, J. Yi, Y. Sohn, J.S. Gwag, Ag nanoparticles decorated ion-beam-assisted TiO2 thin films for tuning the water splitting activity from UV to visible light harvesting, Ceramics International 43(15) (2017) 12814-12821.
[41] P. Chaudhary, P.P. Ingole, Multifunctional plasmonic Ag-hematite nano-dendrite electrocatalysts for methanol assisted water splitting: Synergism between silver nanoparticles and hematite dendrites, Int. J. Hydrogen Energ. 43(3) (2018) 1344-1354.
[42] P. Arunachalam, M.S. Amer, M.A. Ghanem, A.M. Al-Mayouf, D. Zhao, Activation effect of silver nanoparticles on the photoelectrochemical performance of mesoporous TiO2 nanospheres photoanodes for water oxidation reaction, Int. J. Hydrogen Energ. 42(16) (2017) 11346-11355.
[43] M.A. Amin, S.A. Fadlallah, G.S. Alosaimi, In situ aqueous synthesis of silver nanoparticles supported on titanium as active electrocatalyst for the hydrogen evolution reaction, Int. J. Hydrogen Energ. 39(34) (2014) 19519-19540.
[44] M.A. Amin, S.A. Fadlallah, G.S. Alosaimi, F. Kandemirli, M. Saracoglu, S. Szunerits, R. Boukherroub, Cathodic activation of titanium-supported gold nanoparticles: an efficient and stable electrocatalyst for the hydrogen evolution reaction, 41 (15) (2016) 6326-6341.
[45] L. Zhou, D.F. Swearer, C. Zhang, H. Robatjazi, H. Zhao, L. Henderson, L. Dong, P. Christopher, E.A. Carter, P. Nordlander, N.J. Halas, Quantifying hot carrier and thermal contributions in plasmonic photocatalysis, Science 362(6410) (2018) 69-72.
[46] J.X. Wang, J. Huang, H.L. Xie, A.L. Qu, Synthesis of g-C3N4/TiO2 with enhanced photocatalytic activity for H-2 evolution by a simple method, Int J Hydrogen Energ 39(12) (2014) 6354-6363.
[47] W.-J. Ong, L.-L. Tan, Y.H. Ng, S.-T. yong, S.-P. Chai, Graphitic Carbon Nitride (g-C3N4)-Based Photocatalysts for Artificial Photosynthesis and Environmental Remediation: Are We a step Closer To Achieving Sustainability?, Chem. Rev. 116(12) (2016) 7159-7329.
[48] B. Chai, T. Peng, J. Mao, K. Li, L. Zan, graphitic carbon nitride (g-C3N4)-Pt-TiO2 nanocomposite as an efficient photocatalyst for hydrogen production under visible light irradiation, Phys. Chem. Chem. Phys. 14(48) (2012) 16745-16752.
[49] H.J. Yan, H.X. Yang, TiO2-g-C3N4 composite materials for photocatalytic H2 evolution under visible light irradiation, J. Alloy Compd. 509(4) (2011) L26-L29.
[50] Q. Luo, L. Zhang, X.F. Chen, O.K. Tan, K.C. Leong, Mechanochemically synthesized m-BiVO4 nanoparticles for visible light photocatalysis, RSC Adv. 6 (2016) 15796-15802.
[51] L. Zhang, Q. Luo, X. Chen, M.S. Tse, O.K. Tan, K.H.H. Li, Y.Y. Tay, C.K. Lim, X. Guo, K.C. Leong, Mechanochemically synthesized CuO/m-BiVO4 composite with enhanced photoelectrochemical and photocatalytic properties, RSC Adv. 6 (2016) 65038-65046.
[52] C. Marchal, T. Cottineau, M.G. Mendez-Medrano, C. Colbeau-Justin, V. Caps, V. Keller, Au/TiO2-gC3N4 Nanocomposites for Enhanced Photocatalytic H2 Production from Water under Visible Light Irradiation with Very Low Quantities of Sacrificial Agents, Adv. Energ. Mater. 8(14) (2018) 1702142.
[53] B. Turan, J.P. Becker, F. Urbain, F. Finger, U. Rau, S. Haas, Upscalling of integrated photoelectrochemical water-splitting devices to large areas, Nat. Commun. 7 (2016) 12681.
[54] M. Schröder, K. Kailasam, J. Borgmeyer, M. Neumann, A. Thomas, R. Schomäcker, M. Schwarze, Hydrogen Evolution Reaction in a Large-Scale Reactor using a Carbon Nitride Photocatalyst under Natural Sunlight Irradiation, Energ. Technol. 3(10) (2015) 1014-1017.

[55] K. Cocq, C. Lepetit, V. Maraval, R. Chauvin, Carbo-aromaticity and novel carbo-aromatic compounds, Chem. Soc. Rev. 44(18) (2015) 6535-6559.
[56] K. Cocq, C. Barthes, A. Rives, V. Maraval, R. Chauvin, Synthesis of Functional Carbo-benzenes with Functional Properties: The C2 Tether Key, Synlett 30(1) (2019) 30-43.
[57] Z. Li, E. Borguet, M. Smeu, M.A. Ratner, A. Rives, V. Maraval, R. Chauvin, Towards graphyne molecular electronics, Nat. Commun. 6 (2015) 6321.
[58] N. Alenzi, W.-S. Liao, P.S. Cremer, V. Sanchez-Torres, T.K. Wood, C. Ehlig-Economides, Z. Cheng, Photoelectrochemical hydrogen production from water/methanol decomposition using Ag/TiO2 nanocomposite thin films, Int. J. Hydrogen Energy 35(21) (2010) 11768-11775.
[59] I. Baglai, M. de Anda-Villa, R.M. Barba-Barba, C. Poidevin, G. Ramos-Ortiz, V. Maraval, C. Lepetit, N. Saffron-Merceron, J.-L. Maldonado, R. Chauvin, Difluorenyl-carbo-benzenes, hydrocarbon quadrupolar chromophores: synthesis, electronic structure, and two-photon absorption properties, Chem. Eur. J. 21 (2015) 14186-14195.
[60] D. Listunov, C. Duhayon, A. Poater, S. Mazères, A. Saquet, V. Maraval, R. Chauvin, Steric/n-electronic insulation of the carbo-benzene ring: dramatic effect of tert-butyl vs phenyl crowns on geometric, chromophoric, redox and magnetic properties, Chem. Eur. J. 24 (2018) 10699-10710.
[61] A. Rives, I. Baglai, V. Malytskyi, V. Maraval, N. Saffron-Merceron, Z. Voitenko, R. Chauvin, Highly π-electron-rich macro-aromatics: bis(p-aminophenyl)-*carbo*-benzenes and their DBA acyclic references, Chem. Commun. 48 (2012) 8763-8765.
[62] I. Baglai, V. Maraval, Z. Voitenko, Y. Volovenko, R. Chauvin, Towards fluorescent indolyl-*carbo*-benzenes, Fr.-Ukr. J. Chem. 1 (2013) 48-53.
[63] C. Barthes, C. Zhu, R. Khodzhaieva, V. Maraval, R. Chauvin, A. Roshal, Spectral properties of Expanded π-systems: light absorption and emission of a tertaphenyl-*carbo*-benzene, manuscript in preparation. presented as a poster in: *Book of the 10th international Chemistry Conference Toulouse-kiev (ICTK-10)*, Toulouse, June 3-5, 2019, Poster no P53. (2019).
[64] P. Alphonse, A. Varghese, C. Tendero, Stable hydrosols for TiO2 coatings, J. Sol-Gel Sci. Technol. 56 (2010) 250-263.
[65] J. Cure, H. Assi, K. Cocq, L. Marin, K. Fajerwerg, P. Fau, E. Beche, Y.J. Chabal, A. Esteve, C. Rossi, Controlled Growth and Grafting of High-Density Au Nanoparticles on Zinc Oxide Thin Films by Photo-Deposition, Langmuir 34(5) (2018) 1932-1940.
[66] L. Leroyer, C. Zou, V. Maraval, R. Chauvin, Synthesis and stereochemical resolution of a [6]pericyclynedione: Versatile access to pericyclynediol precursors of carbo-benzenes, Comptes Rendus Chimie 12(3-4) (2009) 412-429.
[67] J. Cure, Y. Coppel, T. Dammak, P.F. Fazzini, A. Mlayah, B. Chaudret, P. Fau, Monitoring the Coordination of Amine Ligands on Silver Nanoparticles Using NMR and SERS, Langmuir 31(4) (2015) 1362-1367.
[68] M. Horn, C.F. Schwerdtfeger, E.P. Meagher, Zeitschrift für Kristallographie 136 (1972) 273-281.
[69] S. Agarwala, G.W. Ho, Synthesis and tuning of ordering and cristallinity of mesoporous titanium dioxide film, Mater. Lett. 63(18-19) (2009) 1624-1627.
[70] L. Laffont, M. Monthioux, V. Serin, Plasmon as tool for in situ evaluation of physical properties for carbon materials, Carbon 40(5) (2002) 767-780.
[71] P. Longo, R.D. Twesten, J. Olivier, Probing the Chemical Structure in Diamond-Based Materials Using Combined Low-Loss and Core-Loss electron Energy-Loss Spectroscopy, Microsc. Microanal. 20(3) (2014) 779-783.
[72] B. Reznik, M. Fotouhi, D. Gerthsen, Structural analysis of pyrolytic carbon deposits on a planar cordierite substrate, Carbon 42(7) (2004) 1311-1313.
[73] B.N.J. Persson, On the theory of surface-enhanced Raman scattering, Chem. Phys. Lett. 82(3) (1981) 561-565.

[74] I. Romero, J. Aizpurua, W. Bryant Garnett, F.J. Garcia De Abajo, Plasmons in nearly touching metallic nanoparticles: singular response in the limit of touching dimers, Opt. Express 14(21) (2006) 9988-9999.
[75] T. de Freitas Paulo, V. Bernardes-Génisson, V. Maraval, R. Chauvin, manuscript in preparation (2019).
[76] Z.W. Seh, Liu, S., M. Low, S.-Y. Zhang, Z. Liu, A. Mlayah, M.-Y. Han, Janus Au-TiO2 Photocatalysts with Strong Localization of Plasmonic Near-Fields for Efficient Visible-Light Hydrogen Generation, Adv. Mater. 24(17) (2012) 2310-2314.
[77] L. Leroyer, C. Lepetit, A. Rives, V. Maraval, N. Saffon-Merceron, D. Kandaskalov, D. Kieffer, R. Chauvin, From hexaoxy-[6]pericyclines to carbo-cyclohexadienes, carbo-benzenes, and dihydro-carbo-benzenes: synthesis, structure, chromophoric and redox properties, Chem. Eur. J. 18 (2012) 3226-3240.
[78] C. Zhu, A. Poater, C. Duhayon, B. Kauffmann, A. Saquet, V. Maraval, R. Chauvin, Carbo-biphenyls and Carbo-terphenyls: Oligo(phenylene ethynylene) Ring Carbo-mer, Angew. Chem. Int. Ed. 57 (2018) 5640-5644.
[79] M.V. Roldan, N.S. Pellegri, O.A. de Sanctis, Optical response of silver nanoparticles stabilized by amines to LSPR based sensors, Procedia Materials Science I (2012) 594-600.
[80] T. Takata, K. Domen, Particulate Photocatalysts for Water Splitting: Recent Advances and Future Prospects, ACS Energ. Lett. 4(2) (2019) 542-549.
[81] C. Das, B. Ananthoju, A.K. Dhara, M. Aslam, S.K. Sarkar, K.R. Balasubramaniam, Electron-selective TiO2 / CVD-Graphene Layers for Photocorrosion Inhibition in Cu2O Photocathodes, Adv. Mater. Interfaces 4(17) (2017) n/a.
[82] Y. Tang, X. Hu, C. Liu, Perfect Inhibition of CdS photocorrosion by graphene sheltering engineering on TiO2 nanotube array for highly stable photocatalytic activity, Phys. Chem. Chem. Phys. 16(46) (2014) 25321-25329.
[83] C. Andrei, E. Lestini, S. Crosbie, C. de Frein, T. O'Reilly, D. Zerulla, Plasmonic enhancement of dye sensitized solar cells via a tailored size-distribution of chemically functionalized gold nanoparticles, PLoS One 9(10) (2014) e109836/1-e109836/12.
[84] Z. Yang, P. Zhang, Y. Ding, Y. Jiang, Z. Long, W. Dai, Facile synthesis of Ag/ZnO heterostructures assisted by UV irradiation: Highly photocatalytic property and anhanced photostability, Mater. Res. Bull. 46(10) (2011) 1625-1631.
[85] S.K. Cushing, J. Li, J. Bright, B.T. Yost, P. Zheng, A.D. Bristow, N. Wu, Controlling Plasmon-Induced Resonance Energy Transfer and Hot Electron Injection Processes in Metal@TiO2 Core-Shell Nanoparticles, J. Phys. Chem. C 119(28) (2015) 16239-16244.
[86] M. Wang, J. Han, H. Xiong, R. Guo, Yolk@Shell Nanoarchitecture of Au@r-GO/TiO2 Hybrids as Powerful Visible Light Photocatalysts, Langmuir 31(22) (2015) 6220-6228.
[87] F.-J. Sheu, C.-P. Cho, Investigation of the appropriate content of graphene in Ag-TiO2-graphene ternary nanocomposites applied as photocatalysts, Int. J. Hydrogen Energy 42(27) (2017) 17020-17029.
[88] Z. Wang, Z.-X. Low, X. Zeng, B. Su, Y. Yin, C. Sun, T. Williams, H. Wang, X. Zhang, Vertically-heterostructured TiO2-Ag-rGO ternary nanocomposite constructed with {001} facetted TiO2 nanosheets for enhanced Pt-free hydrogen production, Int. J. Hydrogen Energ. 43(3) (2017) 1508-1515.
[89] T.J. Wong, F.J. Lim, M.M. Gao, G.H. Lee, G.W. Ho, Photocatalytic H2 production of composite one-dimensional TiO2 nanostructures of different morphological structures and crystal phases with graphene, Catal. Sci. Technol. 3(4) (2013) 1086-1093.